Design and fabrication of networks for bacterial computing

Van Delft, Falco C.M.J.M.; Sudalaiyadum Perumal, Ayyappasamy; Van Langen-Suurling, Anja; De Boer, Charles; Kašpar, Ondřej; Tokárová, Viola; Dirne, Frank W.A.; Nicolau, Dan V.

Important note
To cite this publication, please use the final published version (if applicable).
Please check the document version above.

Design and fabrication of networks for bacterial computing

View the article online for updates and enhancements.

New Journal of Physics

The open access journal at the forefront of physics

PAPER

Design and fabrication of networks for bacterial computing

Falco C M J M van Delft[1] [iD], Ayyappasamy Sudalaiyadum Perumal[2] [iD],
Anja van Langen-Suurling[3], Charles de Boer[3], Ondřej Kašpar[2,4] [iD], Viola Tokárová[2,4] [iD],
Frank W A Dirne[3] and Dan V Nicolau[2,*] [iD]

1   Molecular Sense Ltd, Liverpool L36 8HT, United Kingdom
2   Department of Bioengineering, McGill University, Montreal, Quebec, H3A 0C3, Canada
3   Kavli Institute of Nanoscience Delft, Delft University of Technology, 2628 CJ Delft, The Netherlands
4   Department of Chemical Engineering, University of Chemistry and Technology, Prague, Prague 6, Czech Republic
*   Author to whom any correspondence should be addressed.

E-mail: dan.nicolau@mcgill.ca

Abstract

Non-deterministic polynomial (NP-) complete problems, whose number of possible solutions grows exponentially with the number of variables, require by necessity massively parallel computation. Because sequential computers, such as solid state-based ones, can solve only small instances of these problems within a reasonable time frame, parallel computation using motile biological agents in nano- and micro-scale networks has been proposed as an alternative computational paradigm. Previous work demonstrated that protein molecular motors-driven cytoskeletal filaments are able to solve a small instance of an NP complete problem, i.e. the subset sum problem, embedded in a network. Autonomously moving bacteria are interesting alternatives to these motor driven filaments for solving such problems, because they are easier to operate with, and have the possible advantage of biological cell division. Before scaling up to large computational networks, bacterial motility behaviour in various geometrical structures has to be characterised, the stochastic traffic splitting in the junctions of computation devices has to be optimized, and the computational error rates have to be minimized. In this work, test structures and junctions have been designed, fabricated, tested, and optimized, leading to specific design rules and fabrication flowcharts, resulting in correctly functioning bio-computation networks.

1. Introduction

Combinatorial mathematical problems, including nondeterministic polynomial-time (NP-) complete problems, have a number of possible solutions that increases exponentially with the problem size, which, in turn, makes them intractable for conventional *sequentially* operating electronic computers [1–5]. Next to DNA computing, which requires impractically large amounts of DNA when scaling up [6–9], and quantum computing, which appears to be limited in scale by de-coherence and by the small number of qubits that can be integrated [10], massively parallel computation employing motile biological agents in networks has been proposed to solve such problems [11]. This computational paradigm comprises several stages. First, the mathematical problem to be solved must be formalized in a graph, which is subsequently translated in the design of a network that physically encodes this mathematical problem. Next, the fabricated network is exposed to the random, parallel exploration by large numbers of motile biological entities, preferably small-sized, to increase the density of computation per volume, and rapid, to increase the speed of computation. The solutions of the problem can be then derived from the end points and trajectories of the agents in the network.

Previously, one of the classical NP-complete problems, i.e. the subset sum problem (SSP), was encoded into a graphical, modular, planar network comprising logical operational gates, i.e. 'split junctions' and

'pass junctions' [12]. Pass junctions consist of orthogonal crossings aiming to enforce the unperturbed directional passage of the intersecting pathways, whereas in the split junctions this crossing is additionally equipped with two Y-shaped bifurcations to enable the unbiased changing of traffic direction. A small SSP instance was embedded in a nanofabricated planar device, which was explored in a parallel fashion by a large number of cytoskeletal filaments, i.e. actin filaments, or microtubules. The motility of the computing agents was provided by protein molecular motors, i.e. myosin, or kinesin, respectively, which were attached to the bottom (and lateral walls) of the network channels, and which were in contact with an ATP-rich solution above the channels [12].

Autonomously moving bacteria are interesting alternatives to the motor-driven filaments for exploring such channel devices, especially if cell division during exploration could be employed to increase the number of agents in a diverging network [13, 14], while preferably keeping the agent density constant during operation [14]. *E. coli* HCB437, a prokaryotic bacterial species, genetically engineered to have smooth swimming ability and impaired sensory receptors [15–18], is the agent of choice in the present study aiming to explore alternative designs of the SSP 'computer'. The *E. coli* cell is approximately 1 μm wide and 2 μm long, and its effective total length, i.e. cell plus propelling peritrichous flagella, is approximately 4–5 μm. *E. coli* is also known to be motile even in channels only 30% wider than its own diameter [19].

Although the widths and depths of the channels required to accommodate bacteria are typically larger than 1 μm, here nanometre-capable electron beam lithography was chosen in the network fabrication flowchart, against sub-micrometre-capable optical lithography, for the following reasons: (i) in prototyping and optimization studies like the one performed here, electron beam lithography is much more flexible and cost-effective, because one-time usage of expensive optical lithography masks is circumvented; (ii) we wanted to be able to explore sharp features (with a radius of curvature ideally up to 100 times smaller than the channel width) for optimizing pass junctions and bacterial traps (see below); (iii) some cell types, much larger than bacteria, are known to explore their surroundings by using focal adhesion points, and are able to detect/resolve/discriminate nano-scale details in their surroundings, and respond accordingly [20, 21]. Consequently, nano-scale fabrication accuracy was considered essential, even for micro-scale features [22, 23]. As will be discussed below, high aspect ratios of channel profiles proved to be critical, requiring the usage of reactive ion etching to obtain anisotropic etch profiles (in the casting master features). Another important fabrication condition in this study is that the networks should be fabricated in optically transparent materials, in order to be able to monitor the bacterial behaviour by optical microscopy.
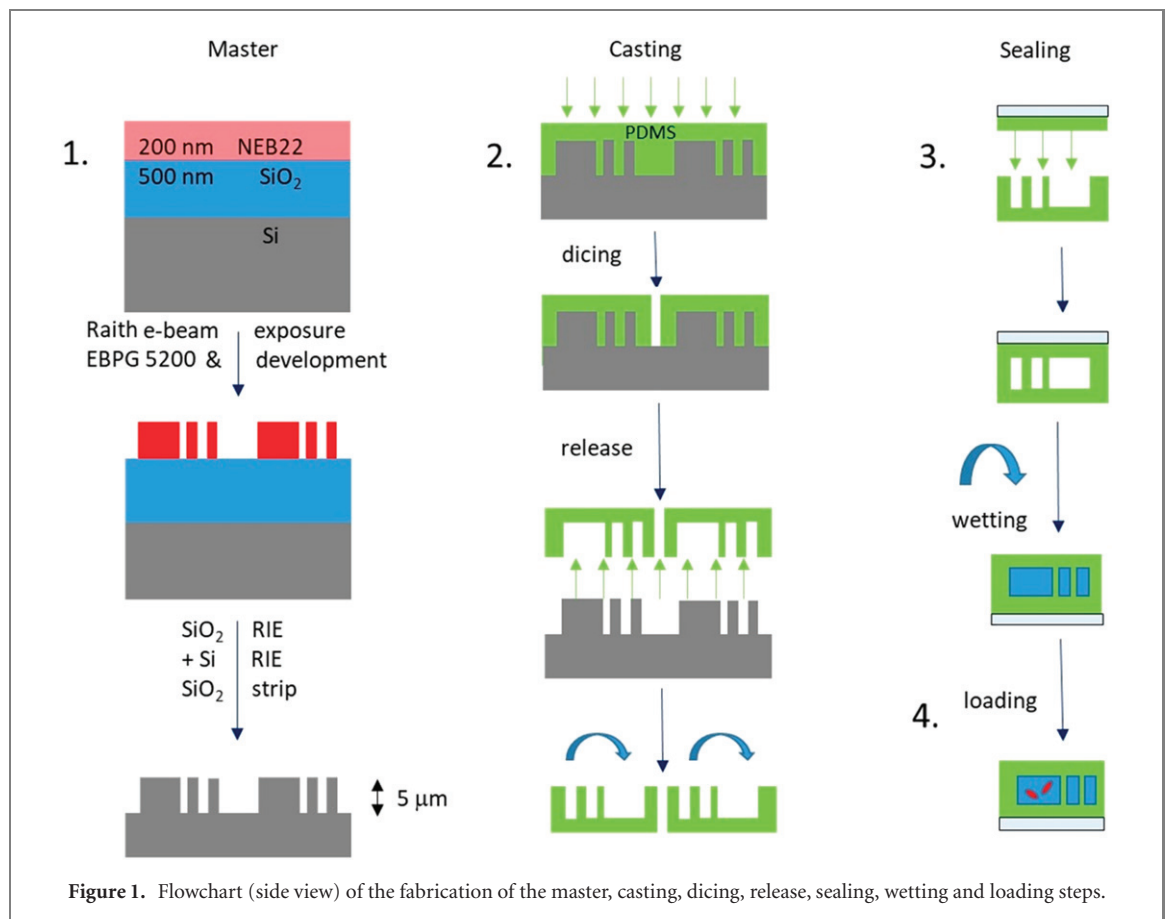
Before designing, constructing, and scaling up the actual computation networks for this bacterial computational agent species, the geometries of the logical junctions must be optimized to achieve the lowest possible error rates, leading to bacteria-specific design rules. This study is necessary as the behaviour of bacteria in micro-confined environments is not fully understood to a level where *ab initio* designs can be proposed [13, 23]. Consequently, the goals of the present work were: (i) to describe the optimised fabrication of such bacterial computing devices; (ii) to study the behaviour of bacteria in different geometrical structures, e.g. wave-shaped channels, sharp-edged zig-zag lines, arrow profiles, etc; (iii) to establish design rules for bio-computation networks; and (iv) to optimize the design of the logic junctions to be employed in future scaled-up bacterial-based network computers.

2. Materials and methods

The above considerations resulted in the following four-stages fabrication flowchart, presented schematically in figure 1:

2.1. Fabrication of a monolithic casting master in silicon

(i) A 500 nm thick SiO_2 layer was deposited on a 100 mm ('4 inch') silicon wafer by plasma enhanced chemical vapour deposition at 300 °C; (ii) hexamethyldisilazane (HMDS) was spin-coated on the wafer at 2000 rpm, which was subsequently baked on a hotplate at 200 °C for 2 min; (iii) a 200 nm thick layer of a negative tone electron beam resist (NEB22, from Sumitomo Corp.) was spin-coated on the wafer, which was subsequently pre-baked on a backing plate in an oven at 110 °C for 2 min; (iv) electron beam exposure of graphic design system (GDS II) patterns was performed on a VISTEC/Raith electron beam pattern generator EBPG-5200 system, at 100 kV, with a 17 μC cm^{-2} dose; for coarse patterns the exposure parameters were: 100 nm beam step size, 150 nm spot size (52 nm defocus) and 148 nA beam current, while for fine patterns these were: 25 nm beam step size, 40 nm spot size (8 nm defocus) and 7 nA beam current; (v) post-exposure bake was performed on a backing plate in an oven at 105 °C for 2 min; (vi) vertical development of the unexposed areas was performed for 30 s in MF322 (Microposit, Shipley), followed by rinsing the patterns twice for 15 s in fresh MF322:H_2O = 1:10, and then rinsing twice for 15 s in fresh H_2O;

Figure 1. Flowchart (side view) of the fabrication of the master, casting, dicing, release, sealing, wetting and loading steps.

(vii) the wafer was spun dry at 2000 rpm; (viii) SiO_2 reactive ion etch (RIE) was performed in a pre-conditioned AMS 100 I-speeder Bosch system, using a 20 sccm C_4F_8/100 sccm He/10 sccm CH_4 flow, with $RF_1 = 2500$ W, $RF_2 = 300$ W, 100% pumping, with the operational parameters of the SH position source: 120 mm, chuck temperature 0 °C, and etch time 3 min 10 s; (ix) 2 μm deep Si-RIE was performed in an ICP chlorine system, with 9 sccm Cl_2, 1 sccm O_2, 7 μbar, RF power 100 W, chuck temperature 65 °C, and etch time 15 min 18 s; alternatively 5 μm deep Si RIE was performed in an AMS cryo-etcher system with chuck temperature -120 °C, $RF_1 = 1100$ W, LF generator pulsed (40 W 10 ms/0 W 90 ms),100% pumping, using one cycle of 26 sccm O_2/200 sccm SF_6 flow, power 13 s ON + 5 min OFF (cooldown), and six cycles of 28 sccm O_2/200 sccm SF_6 flow, power 15 s ON + 5 min OFF (cooldown); (x) the NEB22 residue was removed in an RIE system with 20 sccm O_2 at 30 μbar, with 50 W RF power 1 min and 30 s etch time; (xi) the SiO_2 residue was removed in a buffered HF solution (1:7) for 2 min and 30 s, followed by demineralized water rinse for 5 min, and spin drying at 3000 rpm; and finally (xii) the inspection of the fabricated structures was performed by scanning electron microscopy (SEM).

2.2. Casting of a PDMS replica from the monolithic Si master, dicing and release
(i) A small amount (0.5–1 ml) of chlorotrimethylsilane in a small glass vessel, was placed together with the silicon wafer in a vacuum chamber. After pump down, the vessel was opened to let silanization take place under the vapours for ∼2 h; (ii) Sylgard 184 kit (polydimethylsiloxane (PDMS)) was mixed in 10:1 ratio (monomer:crosslinker) and stirred ∼3 min; (iii) the PDMS mixture was poured over the master structure (all in a petri dish) and put in a vacuum chamber to remove air bubbles (∼2 h); (iv) the petri dish (master covered with PDMS) was either placed in the oven overnight at 60 °C or kept under room temperature during 2−3 d for curing: (v) the chip was cut around the structure and slowly peeled off from the master (the master was then usually covered with a new PDMS mixture to keep it free from contamination (following steps (ii)−(v)).

2.3. Sealing the replica with an oxygen permeable PDMS cover
(i) The PDMS cast (structure face up) was put, together with a PDMS coated glass coverslip, in a plasma cleaner (Harrick Plasma, PDC-32G), pumped down and exposed to the plasma 30 s−45 s; (ii) under vacuum, the cast was attached to the coverslip and plasma treated during 30 s for sealing; (iii) after the chip had been sealed, a small drop of phosphate-buffered saline medium was placed around the chip (in vacuo)
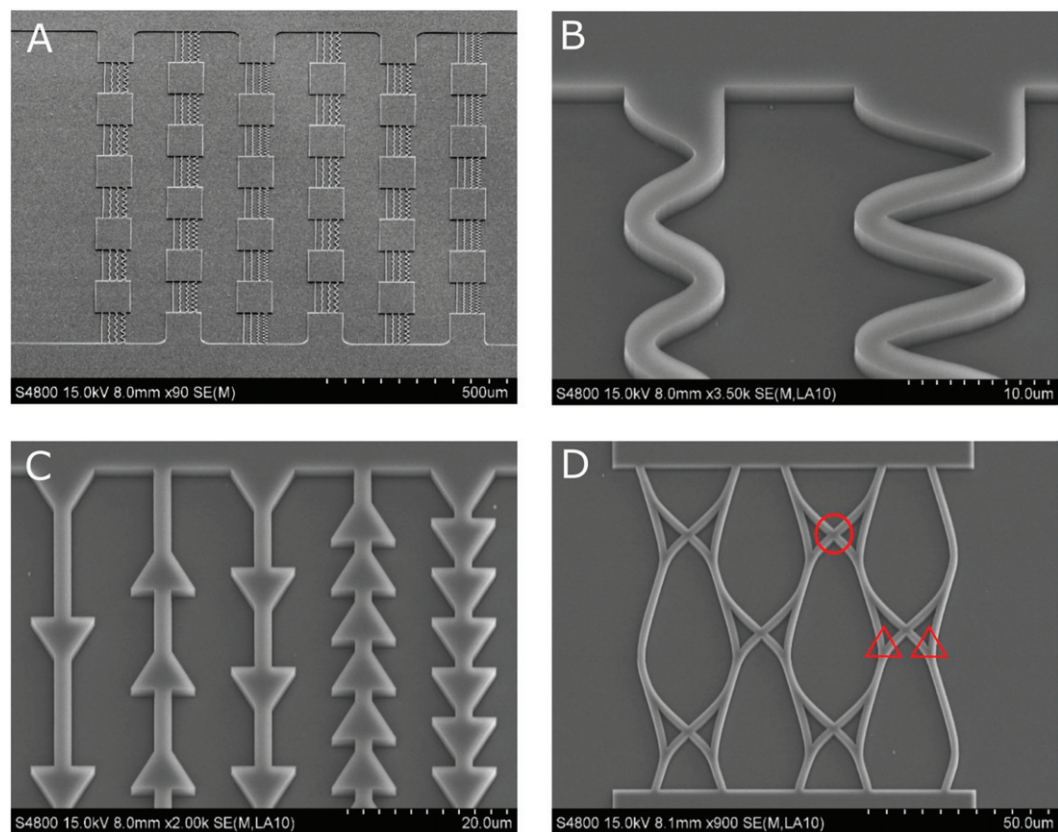
Figure 2. SEM graphs of monolithic Si casting master showing various test structures for 2 μm wide and 2 μm deep channels, obtained using a chlorine ICP system. (A) An overview of lines and curves/waves patterns. (B) Various curves. (C) Various arrows for rectifiers. (D) Pass junctions (indicated by the red circle) and split junctions (indicated by the red triangles).

to assure the medium wetted all structures (at least 5–10 min). The chip was stored in a wet chamber filled with growth medium like luria-bertani medium and refrigerated for future use.

2.4. Loading

Because of its motility characteristics, *E. coli* HCB437 was chosen to test the designs of the bio-computation networks [17, 18]. The *E. coli* cells were transformed to constitutively express the plasmid pMF440mChe (Addgene Plasmid #62 550). Plasmid pMF440mChe was isolated from the *E. coli* DH5α using Qiagen plasmid prep kits (plasmid supplied in transformed *E. coli* DH5α). These isolated plasmids were transformed into the chemically competent cells of *E. coli* HCB437 following a transformation protocol [24]. The bacteria were positively selected using ampicillin (final concentration-100 μg ml^{-1}) to maintain the plasmid and expressed constitutively in the further sub-culturing.

The top edge of the cover-slip-sealed microfluidic device was submerged in a $\sim$50 to 100 μl bacteria-containing solution. Bacteria enter through the edge openings in the loading zone and navigate towards the entry funnel shown below in figure 7. Since the device is entirely operated by the autonomous motility of bacteria, no external force is applied to the device to let the bacteria enter the network.

2.5. Detection

The bacterial culture was examined for red fluorescence using an OlympusIX83 fluorescence microscope with mChe filter. *E. coli* HCB437 transformed with green fluorescent protein (GFP) was also employed, using the plasmid pBAD-EGFP (Addgene plasmid #54 762). Since the tracked signals consisted of grayscale eight-bit images with bright fluorescent spots, both the green and the red fluorescence proteins could be employed here. All images were acquired at either 20 X or 10 X UPLANO objectives with image acquisition performed for 3–5 min. The image acquisition was performed using the Metamorph Advanced Olympus software with an exposure time of 250 ms for each frame (4 fps). The acquired images were post-processed using ImageJ FIJI freeware [25]. The bacterial behaviour was monitored and analysed using ImageJ tracking software with trackmate and MtrackJ plugins [25], and by compilation of fluorescence micrographs.
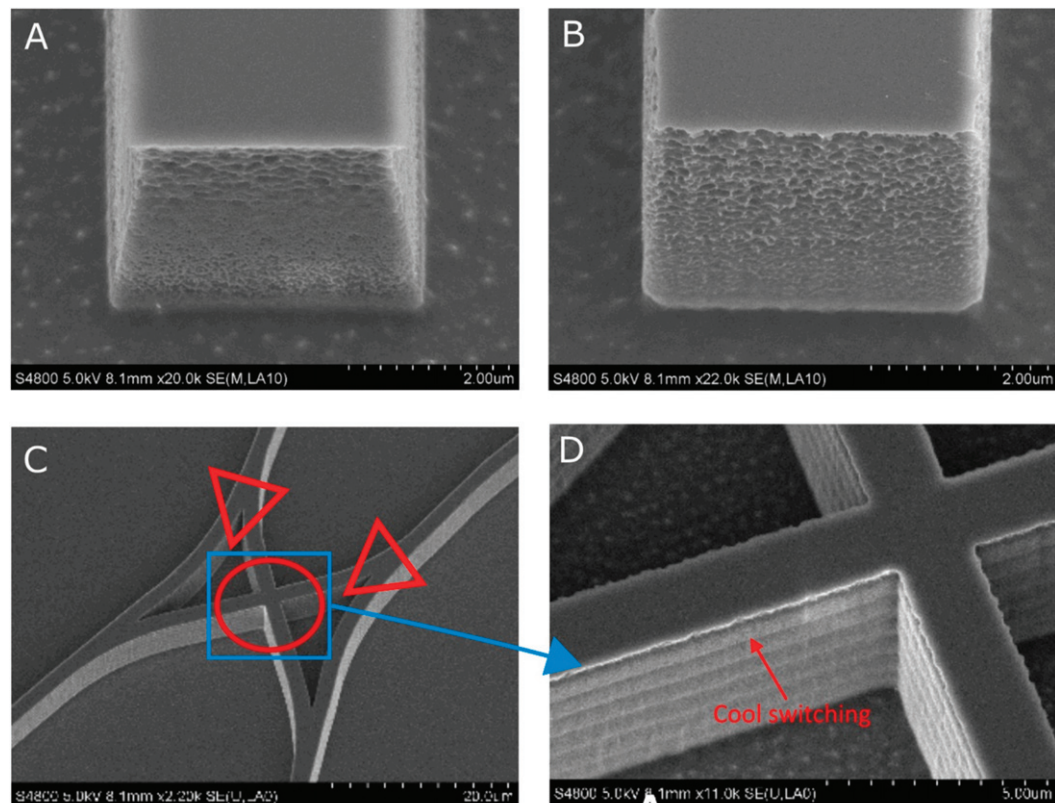
Figure 3. SEM graphs of monolithic Si casting master for 2 μm wide and 5 μm deep channels, obtained using cryo-RIE of Si in a fluorine type of chemistry. (A) Undercut profile with sharp top rim after continuous cryo-RIE. (B) Straight profile after cooldown-interrupted cryo-RIE. (C) Overview of inverted split-junctions (indicated by the red triangles) and pass-junction (indicated by the red circle) after cooldown-interrupted cryo-RIE. The blue rectangle shows the position of (D). (D) Detail of inverted pass junction crossing after cooldown-interrupted cryo-RIE. Minor undulations are visible on the side walls due to the 'cool switching' method.

3. Results and discussion

3.1. Optimized fabrication

Figure 2 presents various test structures on a 2 μm deep master wafer, obtained by silicon etching in a chlorine ICP system. After casting PDMS replicas and performing the first experiments with *E. coli*, it was concluded that supporting pillars in large open areas, e.g. the loading zones, and deeper channels (i.e. $\sim$5 μm) were necessary to prevent 'roof collapse' due to cohesive forces in the sealing step [22]. However, the prolonged etching time needed to achieve this depth on the master wafer resulted into a systematic deposition of particles, which could not be removed. As an alternative, cryo-etching of Si in a fluorine type of chemistry was tested. While the particle deposition problem was addressed, the releasing of the PDMS cast from the master was very difficult. Beyond 2 μm depth, an undercutting emerged (figure 3(a)), which appeared to block the release from the master after PDMS casting (similar to 'dovetail joints'). The Si etch rate was observed to increase in time, as soon as the undercutting started. These etching-related phenomena could be understood from RIE mechanistic considerations [26]. In previous work on RIE of transition metals, using a Luxtron fluoroptic thermometer, it was shown that plasma etching-generated heat is able to raise the temperature on the wafer surface far above the pre-set cooling (water) temperature of the electrode [27]. Apparently, a constant ion-bombardment-induced anisotropic etch rate competed with an increasing thermally activated (isotropic) etching. In order to solve this problem, instead of changing the etch recipe, the system was allowed to cool down repeatedly: in order to minimize undercutting, while maintaining sufficient etch depth, the RIE procedure was performed in seven short cycles with sufficient cool down time (5 min) in between. This 'cool switching' procedure resulted in the desired profile (figures 3(b)–(d)) with only minor undulations, which did not hamper PDMS cast release.
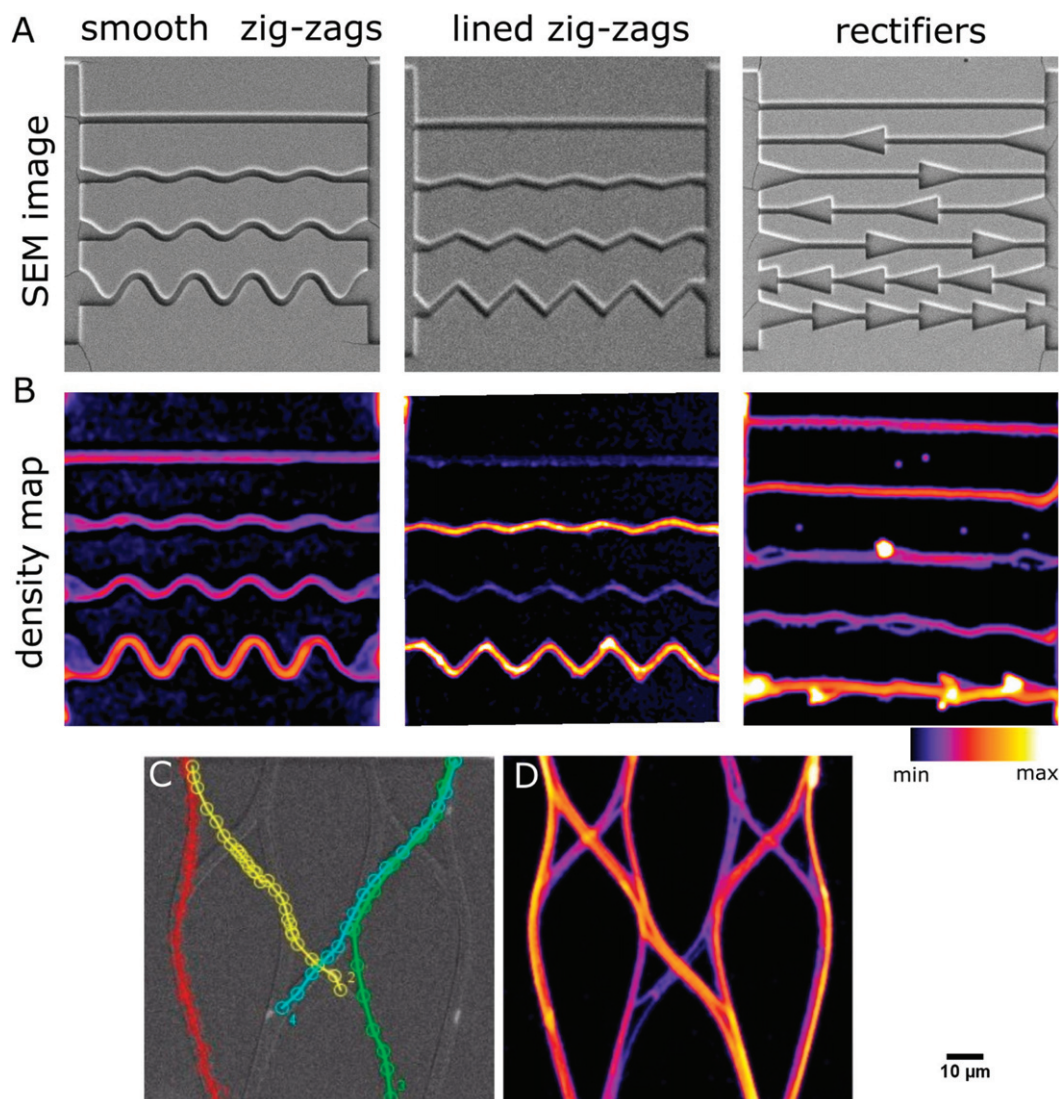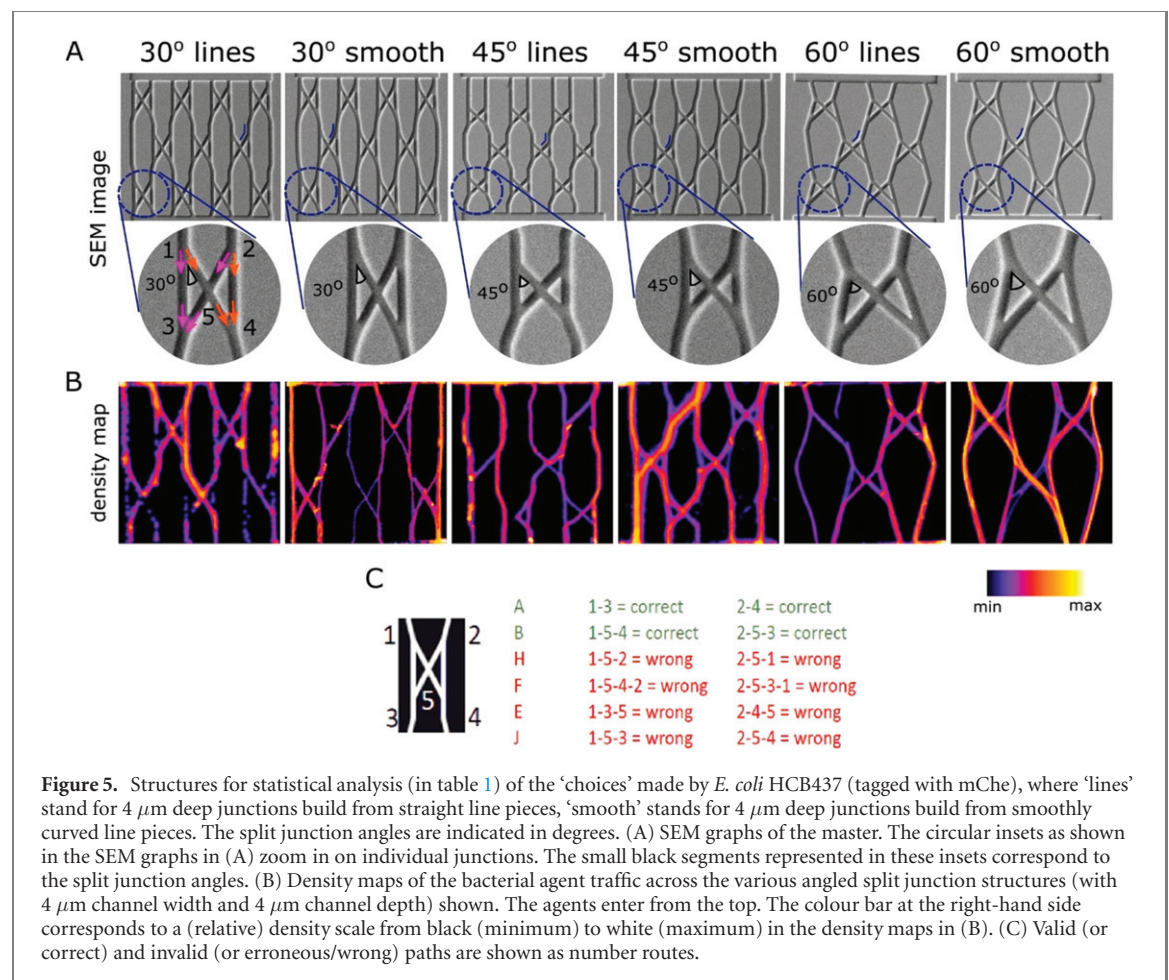
Figure 4. *E. coli* HCB437 motility in various 5 μm deep channel patterns: in waves ((A) and (B)), sharp zigzags, arrows for rectifiers and junctions ((C) and (D)). (A) SEM graphs of the master. (B) Density maps (sum profiles) of the bacterial motility in the corresponding geometries. (C) Bacterial motility in junction monitored using MtrackJ tracking plugin in ImageJ. (D) Sum projections of bacterial motility in junction using fluorescence microscopy. The colour bar at the right-hand side corresponds to a (relative) density scale from black (minimum) to white (maximum) in the density maps in (B) and (D).

3.2. Bacterial motility

Figures 4 and 5 present parts of a sealed PDMS replica with 5 μm deep structures, obtained by cooldown-interrupted cryo-RIE of the casting master wafer. Various PDMS test structures, e.g. waves, sharp zigzags and arrows for rectifiers (figure 4), and split-(and pass) junctions (figures 4 and 5), which are equivalent to the ones presented in figures 2(D) and 3(C) and (D), were explored by *E. coli* HCB437. The inspection of the density maps in figure 4(B) suggests that the sharp zig-zag lines are detrimental to the maintenance of bacterial motility in confined spaces, as these geometries induce corner preferences and clogging, shown as saturated spots at the corners of the arrows and the zig-zag lines. Despite being detrimental to the preservation of motility, which is essential for the operation of logical junctions, this preference of *E. coli* for accumulation in corners and fissures, while avoiding sharp features (angle > 270°), was exploited in other operational instances, e.g. in rectifiers and for trapping bacteria that made errors during computation (described further). In the arrow-shaped rectifiers the bacteria easily move into the direction of the arrow (funnel with angle < 90°), whereas in the opposite direction they need to move between two sharp edges.

Individual bacterial movement was monitored and analysed (figure 4(C)). Subsequently, these individual trajectories, presented as fluorescence micrographs, were aggregated to produce an image of the collective motility behaviour in each test structure (figures 4(B) and (D)). The analysis of the trajectories visualised in figure 4(C) suggest that the design of the split- and the pass junctions translate in the desired

Figure 5. Structures for statistical analysis (in table 1) of the 'choices' made by *E. coli* HCB437 (tagged with mChe), where 'lines' stand for 4 μm deep junctions build from straight line pieces, 'smooth' stands for 4 μm deep junctions build from smoothly curved line pieces. The split junction angles are indicated in degrees. (A) SEM graphs of the master. The circular insets as shown in the SEM graphs in (A) zoom in on individual junctions. The small black segments represented in these insets correspond to the split junction angles. (B) Density maps of the bacterial agent traffic across the various angled split junction structures (with 4 μm channel width and 4 μm channel depth) shown. The agents enter from the top. The colour bar at the right-hand side corresponds to a (relative) density scale from black (minimum) to white (maximum) in the density maps in (B). (C) Valid (or correct) and invalid (or erroneous/wrong) paths are shown as number routes.

bacterial behaviour: (i) in a pass junction the agents cross over along their initial direction (blue–yellow traffic crossing point); and (ii) in a split junction the agents are randomly redistributed between the two forward paths (red–yellow and blue–green traffic split points).

A more detailed inspection of figure 4(D) indicates that the bacteria prefer to move along the edges between the bottom and the walls instead of centred on the axis of the channels, but the individual bacteria can still cross over randomly to the other edge; the random turning left or right at split junctions is still preserved, and the sharp edges at the (pass) crossings prevent the occurrence of wrong turn bends for the 4 to 5 μm long bacteria with flagella.

Figure 5 and table 1 present an analysis of the reliability of the junctions as a function of channel width and height, for various junction geometries. The main conclusions that can be drawn from these results are as follows: (i) for *E. coli*, 2 μm wide channels translate in a considerably better performance than 4 μm wide channels; (ii) smooth structures translate in a considerably better performance than the sharp-cornered structures composed of straight-line pieces at 4 μm channel width; (iii) however, at 2 μm channel width no significant difference is apparent.

3.3. Junction performance and design rules

A more detailed discussion is required to consider the movement of bacteria in the *volume* of the channel, as opposed to just planar projections of trajectories (figure 6(A)). Indeed, the optimum width and depths of the channel highly depend, in the first instance, on the dimensions of the computational agent being used. As noted before, the dimensions of *E. coli* are, approximately, 1 μm for width of the cell, 2 μm for its length, and 4–5 μm for the effective total length of the bacterium, that is, including its propelling peritrichous flagella. These dimensions suggest that, for *E. coli*, a 2 μm channel width is a good choice to prevent U-turn movements. *E. coli* is motile already in channels only 30% wider than its own diameter [19], on the other hand, in order to be effective in avoiding errors, especially in pass junctions, the channel width should not be much larger than twice the agent width.

The channel depth, however, should be more than 2 μm to account for the difficulties related to fabrication of PDMS structures, i.e. roof collapse due to cohesive forces in the sealing step, but not more than 4–5 μm to prevent 'tumbling-over' of bacteria, i.e. vertical switching to the opposite direction (see

Table 1. Comparison of agent traffic behaviour in combined pass- and split-junctions, as a function of channel width and height, and for the various junction geometries shown above. The numbers of wrongly turning agents are shown in comparison with the total numbers of agents, and the percentage of correct passes. 'L' stands for junctions build from straight line pieces; 'C' stands for junctions build from smoothly curved line pieces, and the number attached shows the split junction angle.

Junction type	L30	C30	L45	C45	L60	C60
Organism: *E.coli* HCB437	**channel width 4 μm, channel depth 4 μm**					
Total # of agents	58	84	34	37	42	104
#Wrong turns (E, F, H, J)	10	7	6	2	6	8
Correct passes (A, B)	83%	92%	82%	95%	86%	92%
Organism: *E.coli* HCB437	**channel width 2 μm, channel depth 2 μm**					
Total # of agents	32	61	27	90	26	26
#Wrong turns (E, F, H, J)	1	0	0	1	1	0
Correct passes (A, B)	97%	100%	100%	99%	96%	100%

Figure 6. (A) Artist impression of 'design rules' for channels, junctions and other structural elements in networks (to be) explored by *E. coli* HCB437. #1 and #2: corner preference and preference along walls; #3 and #4: U-turn hindrance at narrow constrained channel width and optimal channel height; #5: the drawing shows (in top view) the bacterial preference (imaged as density ρ) for corners ($\alpha < 90°$) while avoiding sharp features ($\alpha > 270°$). This collective corner preference is used for trapping bacteria in the corners at the exits and at the end of the 'ghost lanes'. Figures (B), (C) and (D), show the SEM images of uncovered PDMS devices when bacteria (marked in pink) were exploring a split junction (B), a pass junction (C) and a corner (D).
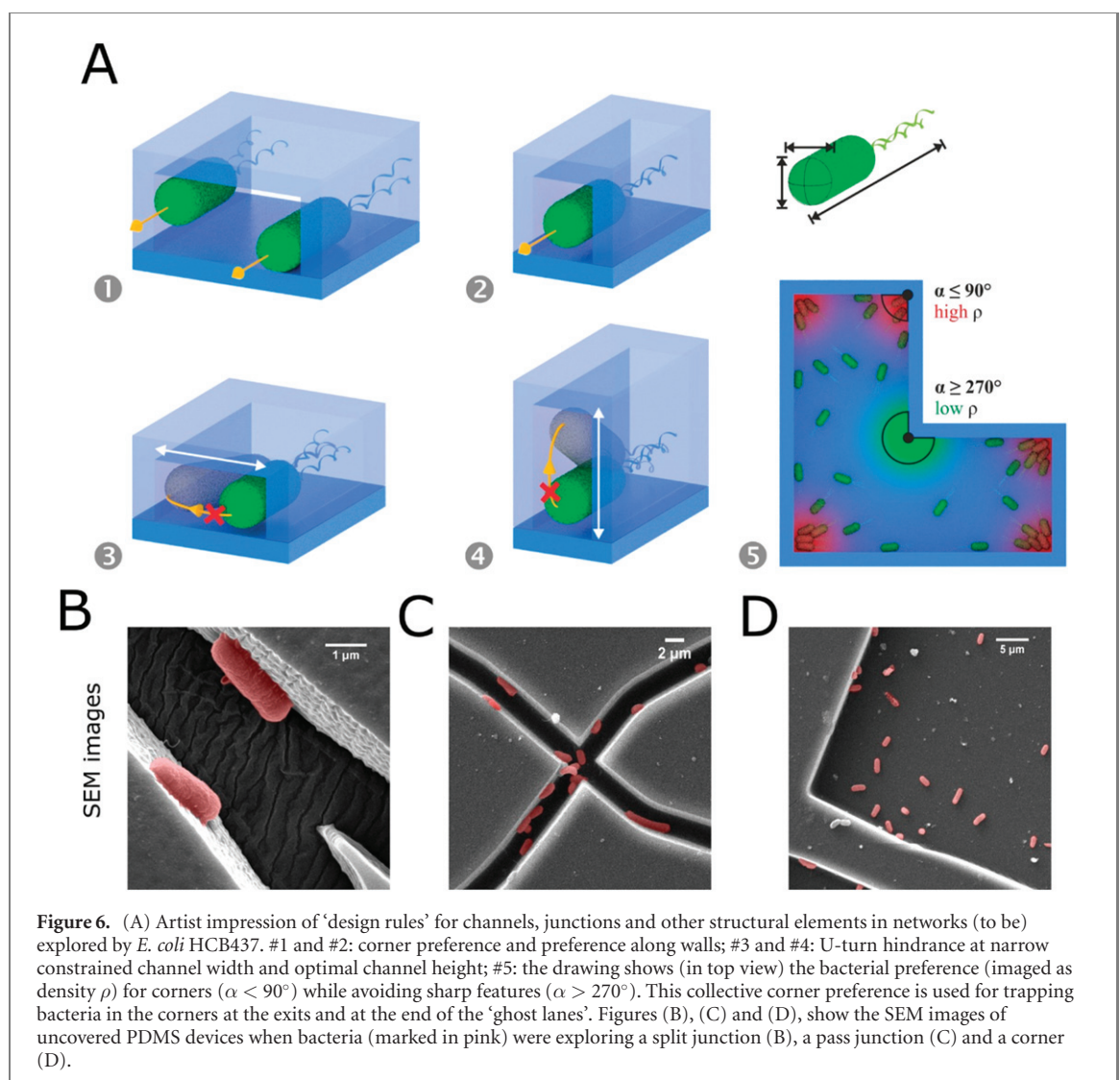
figure 6(A)). These initial considerations based solely on channel and bacterial dimensions, should be augmented with considerations regarding the actual observed motility behaviour of the computational agent. In this context, it was observed in our experiments here that *E coli* swims preferentially along the edges between the walls and the bottom (or the roof) of the confining structure and may even accumulate (clog) in corners [22].
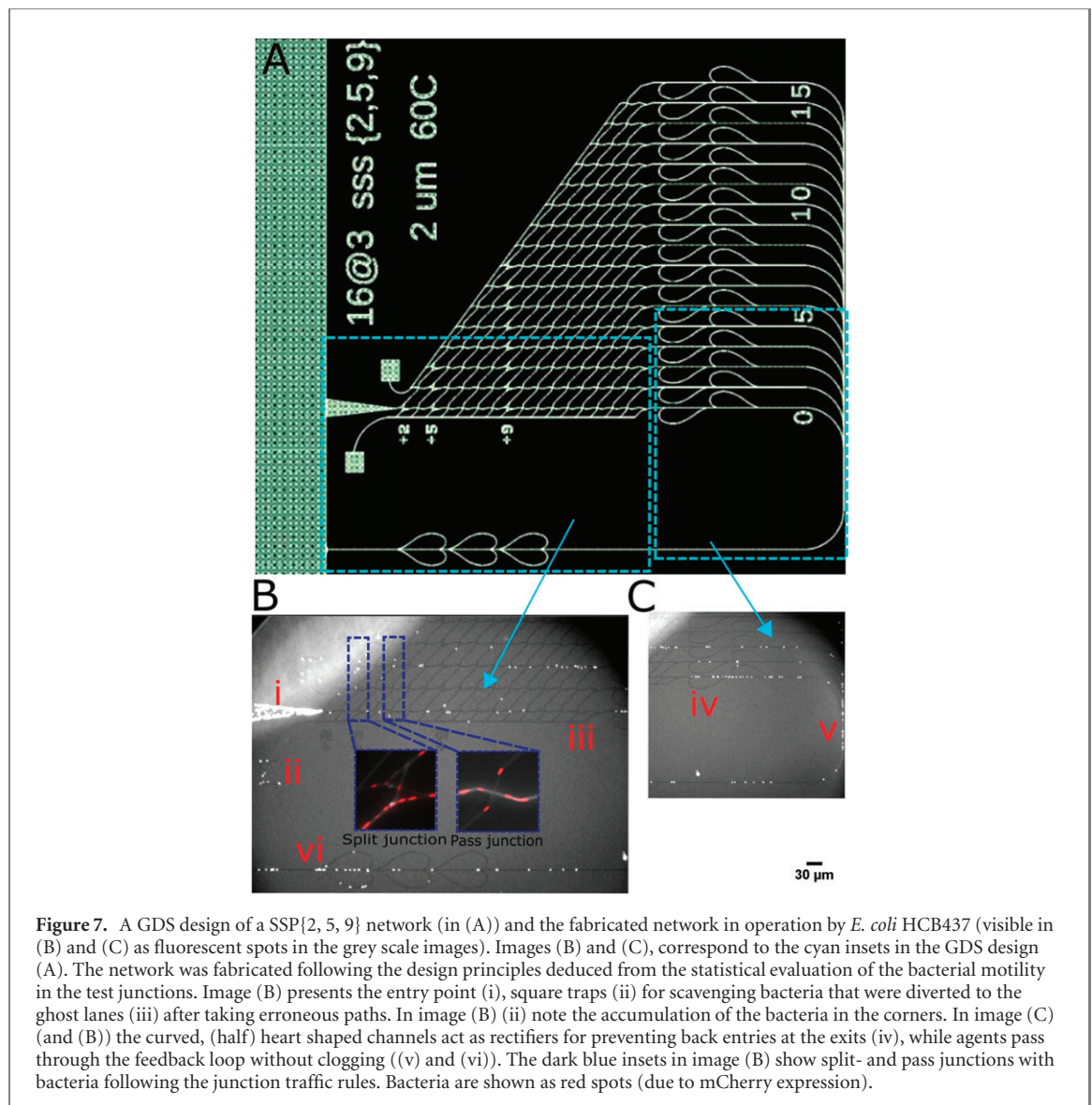
Figure 7. A GDS design of a SSP{2, 5, 9} network (in (A)) and the fabricated network in operation by *E. coli* HCB437 (visible in (B) and (C) as fluorescent spots in the grey scale images). Images (B) and (C), correspond to the cyan insets in the GDS design (A). The network was fabricated following the design principles deduced from the statistical evaluation of the bacterial motility in the test junctions. Image (B) presents the entry point (i), square traps (ii) for scavenging bacteria that were diverted to the ghost lanes (iii) after taking erroneous paths. In image (B) (ii) note the accumulation of the bacteria in the corners. In image (C) (and (B)) the curved, (half) heart shaped channels act as rectifiers for preventing back entries at the exits (iv), while agents pass through the feedback loop without clogging ((v) and (vi)). The dark blue insets in image (B) show split- and pass junctions with bacteria following the junction traffic rules. Bacteria are shown as red spots (due to mCherry expression).

Figures 6(B), (C) and (D) present SEM images of PDMS channels (previously capped but uncovered here for imaging) when bacteria were exploring different sections of the network. Figures 6(B) and (C) represent the bacteria exploring the channels, which can be correlated to the model of bacterial motility constraints, as presented in figure 6(A) 1–4. In addition, corner accumulation of bacteria as depicted in the graphical model (figure 6(A) 5), is observed in the arrows and zig zag channels (figure 4(B)) and in the SEM image (figure 6(D)).

The analysis of all the results for various designs of the logic junctions resulted in a set of design rules, as shown schematically in figure 6:

(a) To prevent turning around of the bacteria and, subsequently, moving in the opposite direction, which is equivalent to 'un-computing' (and can even result in erroneous traffic when turning twice or more), the channel width has to be smaller than the effective bacterial length.

(b) To prevent tumbling-over and moving in the opposite direction, the channel height also has to be smaller than the effective bacterial length.

(c) Furthermore, it was observed that bacteria avoid sharp features, but prefer to move along the edges and into corners and fissures (figures 6(B)–(D)). With increasingly higher densities of bacteria, e.g. by slow movement, possibly coupled with cell division, this behaviour can easily lead to clogging of the network channels. Consequently, designs with sharp corners should be avoided, unless a deliberate trap is needed.

Exploiting these design rules, a network of the small instance SSP{2, 5, 9}, with channel widths of 2 μm and depths of 5 μm was fabricated. This device contains junctions with 60° (split-) and 90° (pass) junction

angles. The graphic design system (GDS II) pattern is presented in figure 7(A). *E. coli* bacteria exploring the network are presented in figures 7(B) and (C). The GDS design was used in the e-beam lithography step in the fabrication process (figure 1). The fabricated bio-computing devices were then exposed to exploration by *E. coli* entering the network through the entry funnel (figure 7(B) (i)) and leaving the network through the (half) heart-shaped rectifiers (figure 7(C) (iv) and figure 7(B) (vi)), following the feedback loop (figure 7(C) (v)) into the loading zone. In principle, the rectifier channels and feedback loop can be replaced by 'exit trap' squares. Bacteria that make a wrong turn, i.e. do not obey the traffic logic rules embedded in the junctions, can be diverted to the 'dirt'- or 'ghost' lanes (figure 7(B) (iii)), and then into square traps (figure 7(B) (ii)). In figure 7(B), the white spots represent the bacteria in the network. It can be noticed that, in the square traps the fluorescence grayscale spots are accumulated in the corners, in accordance with the corner preference. Figures 7(B) and (C) are only snapshots of the bacteria in action, but the successful operation was recorded as a video, and the post-image processing analysis is presented in supplementary information (https://stacks.iop.org/NJP/23/085009/mmedia) movie 1. A dynamic bar chart corresponding to the evaluation of bacteria that explored solutions is also presented in the same supplementary information movie-1. The dynamic bar chart shows the number of agents that passed a specific exit, divided by the total number of agents that reached the exits. Note that the correct solutions for this SSP{2, 5, 9} network, i.e. 0, 2, 5, 7, 9, 11, 14 and 16 can indeed be discriminated in the bar chart against erroneous output.

In this paper the emphasis was on design (rules) and fabrication issues. In a forthcoming paper it will be shown that *E. coli* HCB437 bacteria successfully explored several networks, larger than the one shown in figure 7; those networks have also been fabricated according to the design rules presented here.

4. Conclusions

We have designed, successfully fabricated, and optimised the geometry of biocomputation networks, probing the motility behaviour of *E. coli* HCB437 bacteria. The optimum fabrication protocols were established, based on the use of electron beam lithography and RIE etching for creating casting masters with the correct lateral and vertical profiles of the computing network, subsequently replicated in PDMS-made bacterial 'computers', and successfully explored by *E. coli* HCB437. Specific to our interest, we have optimized the design rules for guiding bacterial traffic in computation networks. While the methodology presented here was developed for *E. coli* HCB437-specific computation, it can be equally well applied to the design optimisation of bio-computation networks for other species, as well as for other types of devices, e.g. for studying soil microbiology, water purification, and single-cell genomics, to name a few.

Data availability statement

All data that support the findings of this study are included within the article (and any supplementary files).

ORCID iDs

Falco C M J M van Delft ⬤ https://orcid.org/0000-0002-3234-2211
Ayyappasamy Sudalaiyadum Perumal ⬤ https://orcid.org/0000-0002-1360-9152
Ondřej Kašpar ⬤ https://orcid.org/0000-0001-5353-6069
Viola Tokárová ⬤ https://orcid.org/0000-0002-8740-415X
Dan V Nicolau ⬤ https://orcid.org/0000-0002-9956-0600

References

[1] Garey M R and Johnson D S 1979 *Computers and Intractability* (San Francisco, CA: Freeman)

[2] Karp R M 1972 Reducibility among combinatorial problems *Complexity of Computer Computations* (Berlin: Springer) pp 85−103

[3] Aaronson S 2005 Guest column: NP-complete problems and physical reality *SIGACT News* **36** 30−52

[4] Darmann A, Nicosia G, Pferschy U and Schauer J 2014 The subset sum game *Eur. J. Oper. Res.* **233** 539−49

[5] Caprara A, Kellerer H and Pferschy U 2000 The multiple subset sum problem *SIAM J. Optim.* **11** 308−19

[6] Adleman L M 1998 Computing with DNA *Sci. Am.* **279** 54−61

[7] Braich R S, Chelyapov N, Johnson C, Rothemund P W and Adleman L 2002 Solution of a 20-variable 3-SAT problem on a DNA computer *Science* **296** 499−502

[8] Ouyang Q, Kaplan P D, Liu S and Libchaber A 1997 DNA solution of the maximal clique problem *Science* **278** 446−9

[9] Reif J H 2011 Scaling up DNA computation *Science* **332** 1156−7

[10] Ladd T D, Jelezko F, Laflamme R, Nakamura Y, Monroe C and O'Brien J L 2010 Quantum computers *Nature* **464** 45−53

[11] Nicolau D V, Nicolau D V, Solana G, Hanson K L, Filipponi L, Wang L and Lee A P 2006 Molecular motors-based micro- and nano-biocomputation devices *Microelectron. Eng.* **83** 1582−8

[12] Nicolau D V *et al* 2016 Parallel computation with molecular-motor-propelled agents in nanofabricated networks *Proc. Natl Acad. Sci. USA* **113** 2591−6

[13] Perumal A S, Nayak M, Tokárová V, Kašpar O and Nicolau D V (ed) 2019 Space partitioning and maze solving by bacteria *Int. Conf. Bio-Inspired Information and Communication* (Berlin: Springer)

[14] van Delft F C M J M, Ippoliti G, Nicolau D V, Sudalaiyadum Perumal A, Kašpar O, Kheireddine S, Wachsmann-Hogiu S and Nicolau D V 2018 Something has to give: scaling combinatorial computing by biological agents exploring physical networks encoding NP-complete problems *Interface Focus* **8** 20180034

[15] Darnton N C, Turner L, Rojevsky S and Berg H C 2007 On torque and tumbling in swimming *E. coli J. Bacteriol.* **189** 1756−64

[16] Wolfe A J, Conley M P, Kramer T J and Berg H C 1987 Reconstitution of signaling in bacterial chemotaxis *J. Bacteriol.* **169** 1878−85

[17] Swiecicki J-M, Sliusarenko O and Weibel D B 2013 From swimming to swarming: *E. coli* cell motility in two-dimensions *Integr. Biol.* **5** 1490−4

[18] DiLuzio W R, Turner L, Mayer M, Garstecki P, Weibel D B, Berg H C and Whitesides G M 2005 *E. coli* swim on the right-hand side *Nature* **435** 1271

[19] Männik J, Driessen R, Galajda P, Keymer J E and Dekker C 2009 Bacterial growth and motility in sub-micron constrictions *Proc. Natl Acad. Sci.* **106** 14861−6

[20] van Delft F C M J M *et al* 2008 Manufacturing substrate nano-grooves for studying cell alignment and adhesion *Microelectron. Eng.* **85** 1362−6

[21] Loesberg W, Teriet J, vanDelft FC M J M, Schön P, Figdor C, Speller S, vanLoon J, Walboomers X and Jansen J 2007 The threshold at which substrate nanogroove dimensions may influence fibroblast alignment and adhesion *Biomaterials* **28** 3944−51

[22] Tokárová V *et al* 2021 Patterns of bacterial motility in microfluidics-confining environments *Proc. Natl Acad. Sci. USA* **118** e2013925118

[23] Nayak M, Sudalaiyadum Perumal A, Nicolau D V and van Delft F C M J M (ed) 2018 Bacterial motility behaviour in sub-ten micron wide geometries *16th IEEE Int. New Circuits and Systems Conference (NEWCAS)* (Piscataway, NJ: IEEE)

[24] Sambrook J, Fritsch E F and Maniatis T 1989 *Molecular Cloning: A Laboratory Manual* (New York: Cold Spring Harbor Laboratory Press)

[25] Schindelin J *et al* 2012 Fiji: an open-source platform for biological-image analysis *Nat. Methods* **9** 676−82

[26] van Delft F C M J M 1996 Mechanistic framework for dry etching, beam assisted etching and tribochemical etching *Microelectron. Eng.* **30** 361−4

[27] van Delft F C M J M and Giesbers J B 1993 The etch mechanisms of magnetic materials in an HCl plasma *J. Nucl. Mater.* **200** 366−70